Tuning of the electronic and vibrational properties of epitaxial MoS_2 through He-ion beam modification

To cite this article: Shayani Parida *et al* 2023 *Nanotechnology* **34** 085702

OPEN ACCESS
IOP Publishing
Nanotechnology

Nanotechnology **34** (2023) 085702 (9pp)
https://doi.org/10.1088/1361-6528/aca3af

Tuning of the electronic and vibrational properties of epitaxial MoS_2 through He-ion beam modification

Shayani Parida[1,2], Yongqiang Wang[1,3], Huan Zhao[1], Han Htoon[1], Theresa Marie Kucinski[1], Mikhail Chubarov[4], Tanushree Choudhury[4], Joan Marie Redwing[4,5], Avinash Dongare[2] and Michael Thompson Pettes[1,*]

[1] Center for Integrated Nanotechnologies (CINT), Materials Physics and Applications Division, Los Alamos National Laboratory, NM, United States of America
[2] Department of Materials Science and Engineering, University of Connecticut, CT, United States of America
[3] Materials Science in Radiation & Dynamics Extremes (MST-8), Materials Science and Technology Division, Los Alamos National Laboratory, NM, United States of America
[4] 2D Crystal Consortium–Materials Innovation Platform, Materials Research Institute, The Pennsylvania State University, University Park, PA 16802, United States of America
[5] Department of Materials Science and Engineering, The Pennsylvania State University, University Park, PA 16802, United States of America

E-mail: pettesmt@lanl.gov

Received 19 July 2022, revised 19 October 2022
Accepted for publication 17 November 2022
Published 7 December 2022

Abstract

Atomically thin transition metal dichalcogenides (TMDs), like MoS_2 with high carrier mobilities and tunable electron dispersions, are unique active material candidates for next generation opto-electronic devices. Previous studies on ion irradiation show great potential applications when applied to two-dimensional (2D) materials, yet have been limited to micron size exfoliated flakes or smaller. To demonstrate the scalability of this method for industrial applications, we report the application of relatively low power (50 keV) $^4He^+$ ion irradiation towards tuning the optoelectronic properties of an epitaxially grown continuous film of MoS_2 at the wafer scale, and demonstrate that precise manipulation of atomistic defects can be achieved in TMD films using ion implanters. The effect of $^4He^+$ ion fluence on the PL and Raman signatures of the irradiated film provides new insights into the type and concentration of defects formed in the MoS_2 lattice, which are quantified through ion beam analysis. PL and Raman spectroscopy indicate that point defects are generated without causing disruption to the underlying lattice structure of the 2D films and hence, this technique can prove to be an effective way to achieve defect-mediated control over the opto-electronic properties of MoS_2 and other 2D materials.

Supplementary material for this article is available online

Keywords: mechanical, electronic, vibrational, epitaxial, ion beam modification, optical, two-dimensional

(Some figures may appear in colour only in the online journal)

* Author to whom any correspondence should be addressed.

Introduction

Graphene and analogous two-dimensional (2D) materials, including, hexagonal boron nitrides, transition metal dichalcogenides (TMDs), and MXenes, are ideal candidates for a plethora of applications such as lithium-ion batteries [1,2], flexible transistors [3,4], solar cells [5], catalysis [6], photo detectors [7], active optical components [8–16], and pressure and strain sensors [17,18] due to their unique electrical and optical properties [19–21]. Among these, MoS_2 [22] is a widely studied TMD owing to wide availability of molybdenite ore [23], high in-plane mechanical strength [24] and tunability of band gap with number of layers [25]. The physical features of MoS_2 can be further manipulated by controlling the defect type and density to obtain superior device performance [26–30]. Defects can be introduced in MoS_2 in the growth stage. By adjusting the deposition parameters, Xie *et al* regulated the S and Mo vacancies in MoS_2 grown using pulsed laser deposition [31]. Wu *et al* presented a scheme to control the defect level by introducing hydrogen flow during the chemical vapor deposition process [32]. Several post synthesis techniques have also been employed to introduce defects in MoS_2. Nan *et al* demonstrated significant enhancement of photoluminescence (PL) of monolayer MoS_2 through defect engineering and oxygen bonding [27]. They achieved precise control over the PL signature by annealing the sample in the presence of O_2. Ye *et al* explored the effects of O_2 plasma, as well as H_2 treatment at elevated temperatures on the concentration of edge defects in MoS_2 [33]. Fox *et al* used ultrafine helium ion microscopy to achieve localized tuning of resistivity [34]. Ma *et al* tuned the bandgap of monolayer MoS_2 by substituting S with Se atoms via sputtering process [35], and removed S ions by irradiating the material with Ar^+ ion beam and followed it by introduction of Se precursors. Kwon *et al* demonstrated that the work function of monolayer MoS_2 can be controlled by proton influx [36]. Wang *et al* provided evidence for indirect to direct band gap transition of few layer MoS_2 by proton irradiation [37].

Among these explored techniques, ion irradiation presents the most promising opportunity for wafer-scale control over the process of defect introduction by precise modulation of ion type, accelerating voltage, fluence, etc [38]. He *et al* showed that S vacancy in MoS_2 can be finely tuned by modulating the Au^+ ion fluence between 5×10^{11} to 10^{14} ions cm^{-2}. In another work, Mathew *et al* observed magnetic ordering in MoS_2 flakes upon proton irradiation [39]. This showcased the possibility of using ion irradiation technique for fabrication of spintronic devices by creating magnetic regions in a diamagnetic lattice. Ion irradiation has also been shown as an effective method for reversible amorphization of MoS_2 flakes [40]. Chen *et al* noted the formation of atomistic defects during Ar^+ irradiation of MoS_2 that controlled the band alignment in heterostructures of MoS_2. They combined experiments with simulations to identify the type of point defects formed. Theoretical studies have also revealed the possibility of tuning the properties of TMDs, primarily, by modulating the defect densities, in 2D materials [28,41,42]. More recently, Han *et al* desulphurized the top S layer in monolayer MoS_2 by He^+ ion irradiation [43]. This method yields great potential towards stabilization of metallic phases as well as synthesis of Janus structures of TMDs; MXY, where M is a transition metal, X and Y are chalcogens (S, Se, Te). Overall, these studies indicate that ion irradiation can be effectively used to tune the properties of single or few layers of 2D materials, or their heterostructures, by precise control of the density of defects, and without significant disruption of the film.

Though previous studies on ion irradiation show great potential applications, they are mostly limited to micron size exfoliated flakes or smaller. To demonstrate the scalability of this method for industrial applications, we report the application of ion irradiation towards tuning of the optoelectronic properties of an epitaxially grown continuous film of MoS_2 and demonstrate that precise manipulation of atomistic defects can be achieved even in a wafer scale TMD film using ion implanters, which are routinely used in the semiconductor industry [44,45]. The effect of fluence of $^4He^+$ ions on the PL and Raman signatures of the irradiated film provides new insights into the type and concentration of defects formed in the MoS_2 lattice. Post treatment PL and Raman spectroscopy indicate that point defects are generated without causing disruption to the lattice structure of the thin films and hence, this technique can prove to be an effective way to achieve defect-mediated control over the opto-electronic properties of MoS_2 and other 2D materials.

Methods

Metal organic chemical vapor deposition (MOCVD) growth of monolayer epitaxial MoS_2

Molybdenum disulfide films were synthesized using molybdenum hexacarbonyl [$Mo(CO)_6$, Sigma-Aldrich, >99.9% purity] and hydrogen sulfide (H_2S, Praxair, 99.5% purity) on 2-inch diameter *c*-plane sapphire substrates (Cryoscore Optoelectronic Ltd) in a cold-wall horizontal reactor with an inductively heated SiC-coated graphite susceptor. The MoS_2 growth was carried out at 1000 °C and 50 Torr reactor pressure using UHP hydrogen as the carrier gas. The $Mo(CO)_6$ powder was contained inside a stainless-steel bubbler held at 10 °C and 950 Torr and hydrogen carrier gas was passed through the bubbler at a flow rate of 10 sccm which resulted in a $Mo(CO)_6$ flow rate of 3.6×10^{-2} sccm out of the bubbler. The H_2S flow rate was maintained at 400 sccm throughout the entire growth which was carried out for 18 min.

Ion irradiation

Controllable irradiation was performed using the Danfysik 200 kV research ion implanter at the Ion Beam Materials Laboratory (IBML) at LANL. The chamber pressure was

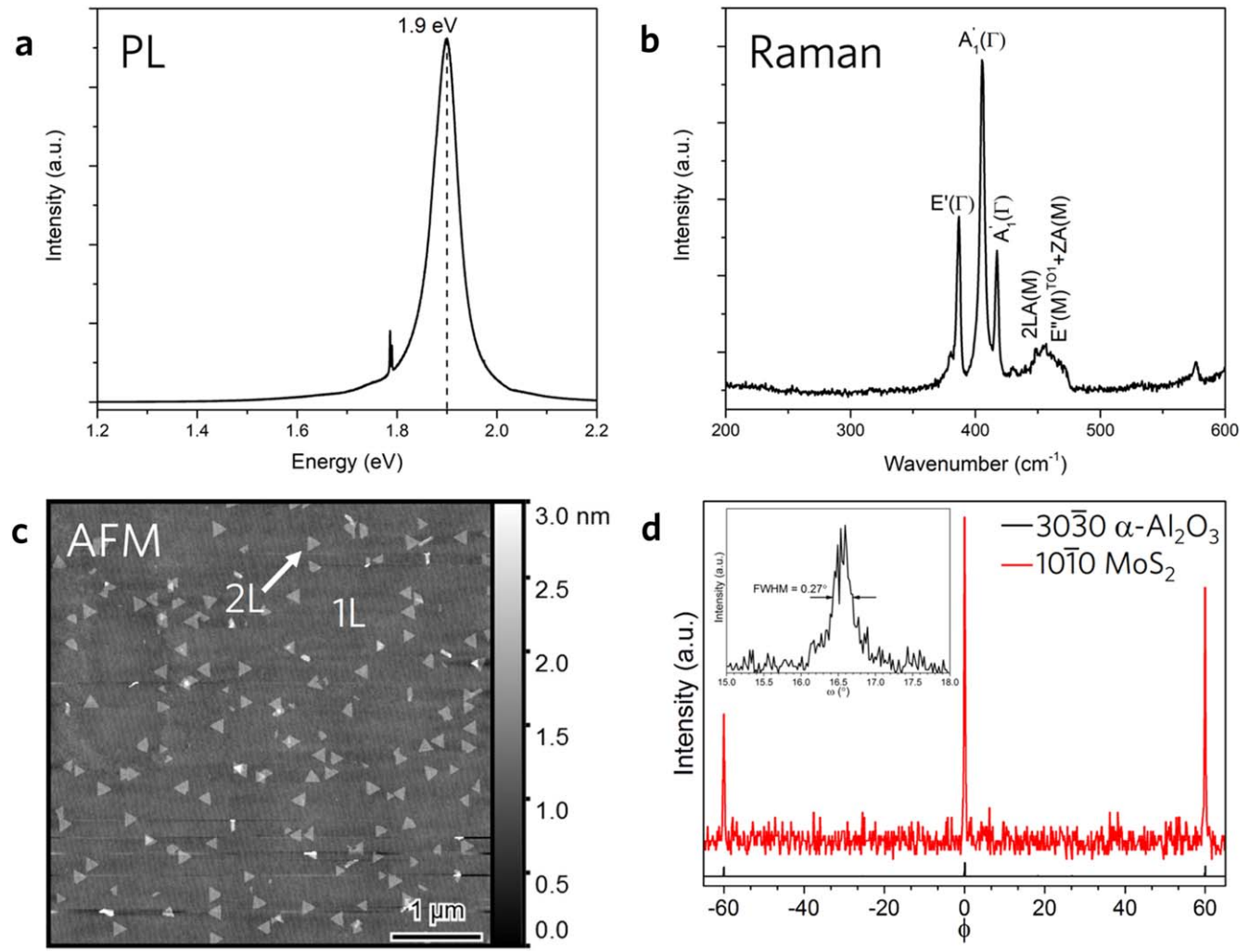

Figure 1. Room temperature as-grown properties of wafer-scale, nominally monolayer epitaxial MoS_2 synthesized on *c*-plane sapphire. (a) Photoluminescence (PL) demonstrates a strong luminescent peak at 1.85 eV and an absence of the indirect transition peak at ∼1.5 eV suggesting a monolayer film. (b) Raman peak relative intensities suggest formation of a monolayer film. Raman and PL were obtained under 532 nm excitation. (c) Atomic force microscopy (AFM) analysis showing large-area coalesced and uniform coverage of predominantly one-layer (1L) MoS_2. Small multilayer regions appear as bright features. (d) In-plane x-ray diffraction ϕ scan demonstrates texture in the epitaxial MoS_2-on-Al_2O_3 film.

maintained at 2.1×10^{-7} Torr and MoS_2 on *c*-sapphire was irradiated with $^4He^+$ (50 keV). Ion fluences for $^4He^+$ irradiation was varied from 1.36×10^{15} to 2.72×10^{16} ions cm^{-2}. Scanning electron microscope (SEM) images were taken of the irradiated samples using a Thermo Fisher Scientific Apreo SEM operated at 1 kV, 12.5 pA beam current, T2 detector, and immersion use case.

Optical characterization

The spatial PL emission and Raman spectra of as-grown and irradiated MoS_2 were performed in reflection mode using the 488.0 nm continuous wave emission line of an Argon ion laser (LEXEL Quantum 8 SHG, Cambridge Laser Laboratories Inc.) and 532.3 nm continuous wave excitation (Oxxius LCX-532S-100, single longitudinal mode diode pumped solid state laser), in a Horiba LabRAM HR Evolution high resolution confocal Raman microscope fitted with volume Bragg gratings. The experiment was configured using a 600 mm^{-1} holographic grating blazed at 500 nm and 300 μm confocal hole diameter for PL and a 2400 mm^{-1} holographic grating blazed at 250 nm and 50 μm confocal hole diameter for Raman. Room temperature measurements conducted in air used an achromat 100×, 0.9 numerical aperture (N.A.) objective (MPLN100X, Olympus). For data collected at 4 K, samples were placed in a variable temperature optical cryostat system (Microstat HiRes, Oxford Instruments) fitted with a 1 mm thick Spectrosil WF window, and used a semi-apochromat 60×, 0.7 N.A. glass corrected objective (LUCPLFLN60X, Olympus). Spectral calibration was performed using the 1332.5 cm^{-1} band [46] of a synthetic Type IIa diamond, and spectral intensity was calibrated using a

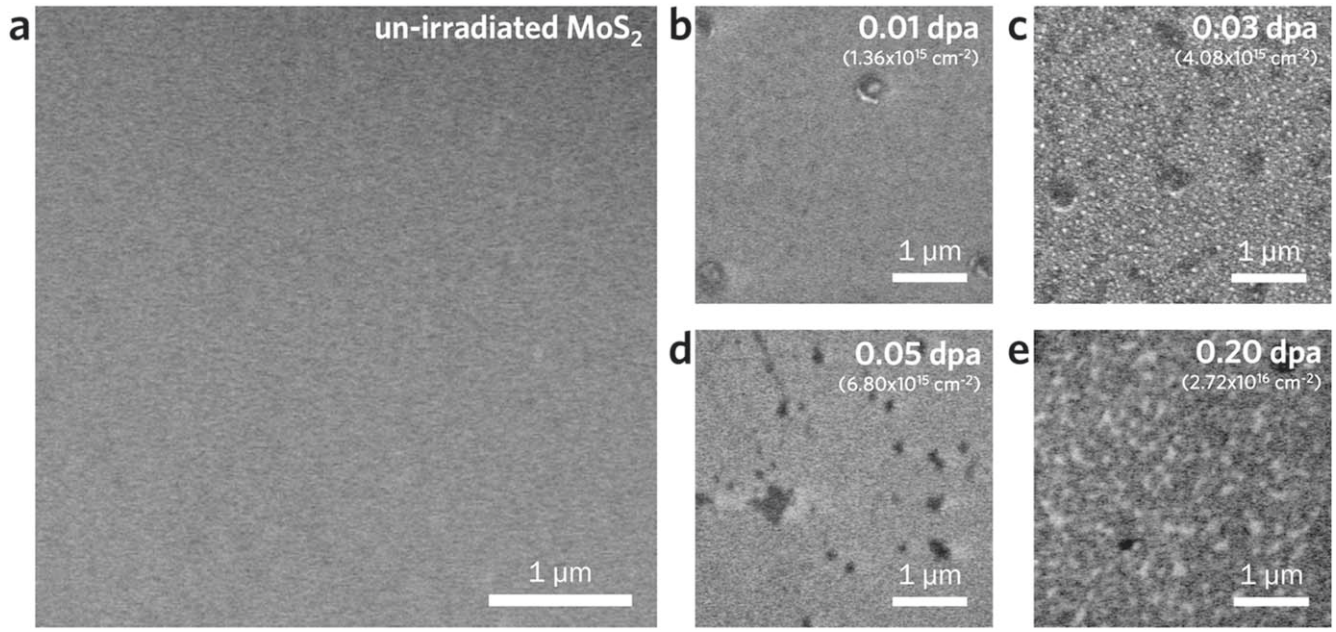

Figure 2. Scanning electron microscope (SEM) images comparing (a) unirradiated and (b)–(e) 50 kV $^4He^+$ irradiated epitaxial MoS_2 on *c*-sapphire. Fluences and corresponding displacements per atom (dpa) are listed in each panel.

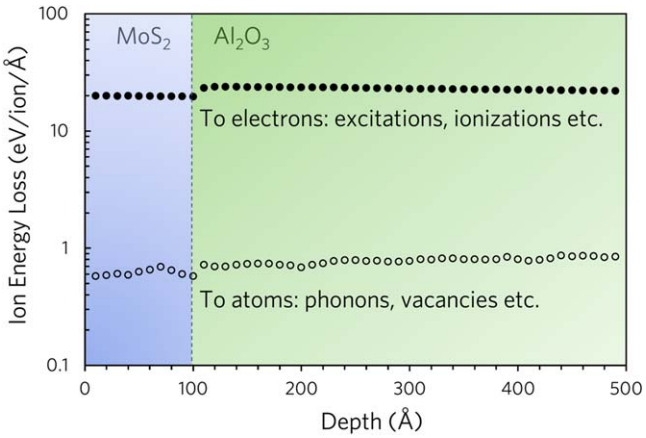

Figure 3. 50 keV He ion energy partitioning in MoS_2 and Al_2O_3 interface region where >87% of the He energy is transferred to target electrons based on our Monte Carlo based stopping and range of ions in matter (SRIM) simulation. We used 10 nm MoS_2 layer (instead of 1 nm monolayer) to get more data points for the 2D layer in SRIM simulations. SRIM simulations (not shown) indicate negligible surface sputtering and helium doping in the 2D layer. In fact, 50 keV He ions fly pass the 2D layer and then rest at 235 nm deep in Al_2O_3 substrate.

VIS-halogen light source (NIST test no. 685/289682–17). Instrumental linewidth broadening was measured using a Hg (Ar) calibration lamp (model 6035, Oriel Instruments) to be ∼0.69–1.00 cm^{-1} for Raman and ∼0.03 nm for PL in the configurations used here.

For time resolved photoluminescence (TRPL), the sample was confocally excited by a 60 ps, 405 nm laser pulses at 3–10 MHz repetition rate through a 50×, 0.7 N.A. objective. The excitation power was ∼100 μW. The collected PL was spectrally filtered using a 620 nm long-pass filter and a 690 nm short-pass filter and detected by an avalanche photodiode with 16 ps time resolution. Time response statistics were obtained with a HydraHarp 400 time-correlated single photon counting system.

Mass spectrometry of MOCVD MoS_2

Rutherford backscattering spectrometry (RBS) was conducted on a National Electrostatics Corporation 3 MV tandem accelerator using a 2 MeV $^4He^+$ ion beam. A solid-state silicon detector located at 167° from the beam direction was used to detect the scattered He particles. A bismuth-implanted silicon standard was used as a reference to minimize uncertainty in the charge collection and the solid angle determination, and 2 MeV was found to work well for this sample.

Quantum mechanical simulations

First principles quantum mechanical simulations were performed within the density functional theory (DFT) framework using Vienna *Ab initio* Simulation Package [47]. The wave function was described by a basis set of plane waves with energy cut-off of 500 eV. The generalized gradient approximation formulated by Perdew–Burke–Ernzerhof was used to represent electronic exchange correlation [48]. Electron-ion interaction was described by the projector augmented-wave method [49]. The reciprocal lattice was sampled using 14 × 14 × 1 grid and 15 Å vacuum was introduced to minimize interlayer interactions. The cell parameters were optimized by using the conjugate gradient scheme such that forces in each direction were below 0.1 eV $Å^{-1}$. A defected MoS_2 structure was created by removing one S atom in a 2 × 2 × 1 supercell of MoS_2 (figure S1, supporting information) and relaxing the resultant structure. This results in the stoichiometry of $MoS_{1.75}$. The band structures and the Raman spectroscopy were plotted using the Phonopy package [50].

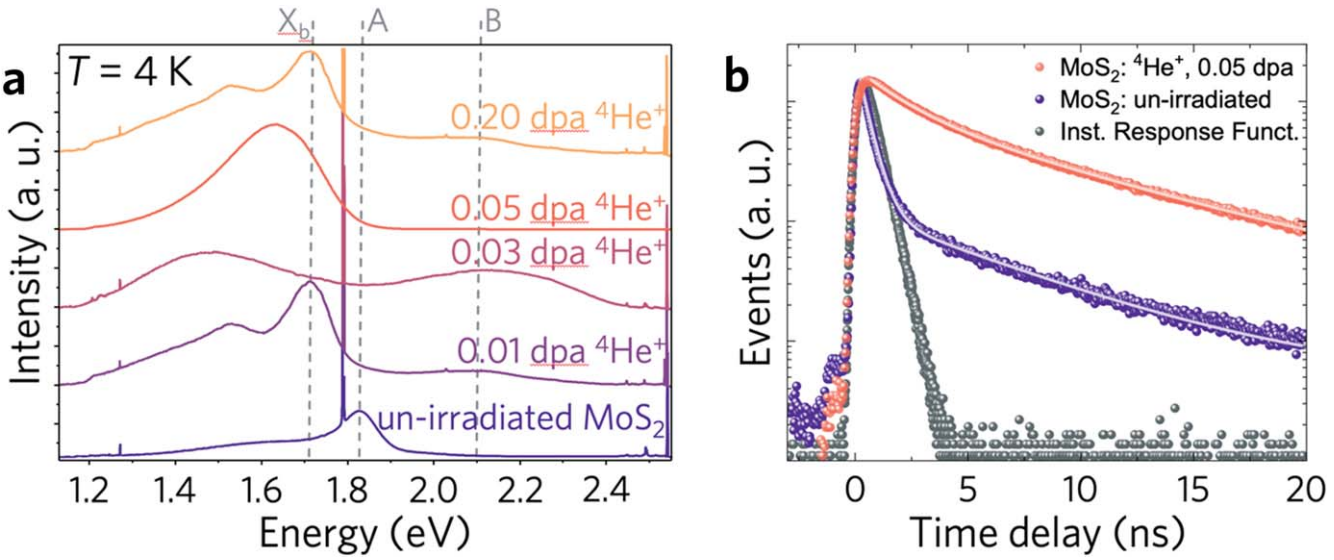

Figure 4. (a) PL spectra of MoS_2 irradiated by $^4He^+$ ion beams with different fluences given in displacements per atom (dpa) show emergence of the bound exciton, X_b, peak at ~1.7 eV upon irradiation attributed to generation of point lattice defects. Spectra are shown normalized to the intensity of sapphire peaks and were recorded at 4 K. (b) Time resolved PL of pristine and irradiated MoS_2. The fast exciton decay time increases orders of magnitude upon ion irradiation owing to exciton localization at defect sites.

Results and discussion

Wafer scale MoS_2 was grown epitaxially on a *c*-Al_2O_3 (*c*-sapphire) substrate using MOCVD. Figure 1(a) demonstrates a strong PL peak at 1.9 eV and was absent of a peak at 1.5 eV which indicated that the sample was primarily monolayer 2H-MoS_2. RBS was performed to quantify defects and impurities present in the sample as it has been shown to be very sensitive to stoichiometry [10,11,51], as shown in (figure S2, supporting information). Upon analyzing the scattering yield ratio of Mo and S, the Mo:S ratio of the un-irradiated sample was obtained to be 1:2.11. This indicates a fairly defect free MoS_2 with the possibility of presence of either a few Mo vacancies (~5.2% Mo vacancies) or excess S atoms in the lattice. The latter is more likely since the film was grown in a highly S-rich condition. Previous studies have suggested that the ratio of intensity of the longitudinal acoustic phonon at the Brillouin zone edge [M-point, LA(M)] peak to the first order peaks at the Brillouin zone center (Γ-point) gives insights into the extent of defects present in the sample, where a higher ratio is associated with more defects [52]. The Raman spectra of figure 1(b) shows the intensity of the 2LA(M) peak is quite weak compared to the first order peaks [$A'(\Gamma)$ and $E'_1(\Gamma)$] which further provides evidence that the wafer scale MoS_2 sample was relatively homogenous and defect free. Figure 1(c) presents AFM characterization showing that the sample was mostly monolayer with some small bi-layer crystals nucleated on the surface. The crystallinity and epitaxial nature of the as-grown sample was confirmed by the sharp peaks seen in the XRD shown in figure 1(d).

Irradiation of the monolayer MoS_2 film with $^4He^+$ ions can lead to defect generation and a swelling of the substrate, the nature of which would depend on the type fluence of the ions used. To investigate this phenomenon, the MoS_2 samples were irradiated with 50 kV $^4He^+$ at different fluences to study the effect of ion dosage: 1.36×10^{15} $ionsc^{-1}\,m^{-1-2}$ [0.01 displacements per atom (dpa)], 4.08×10^{15} $ionsc^{-1}\,m^{-1-2}$ (0.03 dpa), 6.80×10^{15} $ionsc^{-1}\,m^{-1-2}$ (0.05 dpa), and 2.72×10^{16} $ionsc^{-1}\,m^{-1-2}$ (0.20 dpa). Figure 2 shows SEM images of the post irradiated samples showing that the morphology MoS_2 film remains intact after ion irradiation but at higher irradiations, sub-micron sized voids can be seen in the film. Additionally, figure 3 presents Monte Carlo simulations were performed to understand the energy loss profile of the incident ions as they travel through the MoS_2 film. The analysis shows that at 50 keV, very little energy would be transferred from the ions to the film resulting in minimal damage to the surface.

At 4 K, the un-irradiated MoS_2 sample showed a PL peak at 688 nm [figure 4(a)] corresponding to the monolayer MoS_2 band gap of 1.9 eV. In monolayer MoS_2, direct electronic transition is possible at the K-point of the Brillouin zone, and this results in two excitonic peaks: *A* (around 1.9 eV) and *B* (around 2.1 eV). The splitting of the transition peak is due to spin–orbit coupling. In a defect free MoS_2 sample, the *B* peak is almost non-existent when compared the *A* peak, as seen in figure 4(a). Upon ion irradiation, the *B* peak becomes more prominent, and this can be attributed to formation of defects. Previous studies have suggested that a higher B/A peak intensity ratio indicates high defect density in the sample [53]. Additionally, a prominent X_b peak is seen around 1.75 eV which can be attributed to bound excitons formed due to generation of point defects [38]. A previous DFT study showed that the X_b peak is primarily attributed to the formation of di-sulfur vacancy defects [26]. The formation of defects creates additional states for electron occupancy in the band gap and thus can facilitate electronic transitions and consequent formation of bound electron–hole pairs at lower energies. The sample irradiated at 0.05 dpa $^4He^+$,

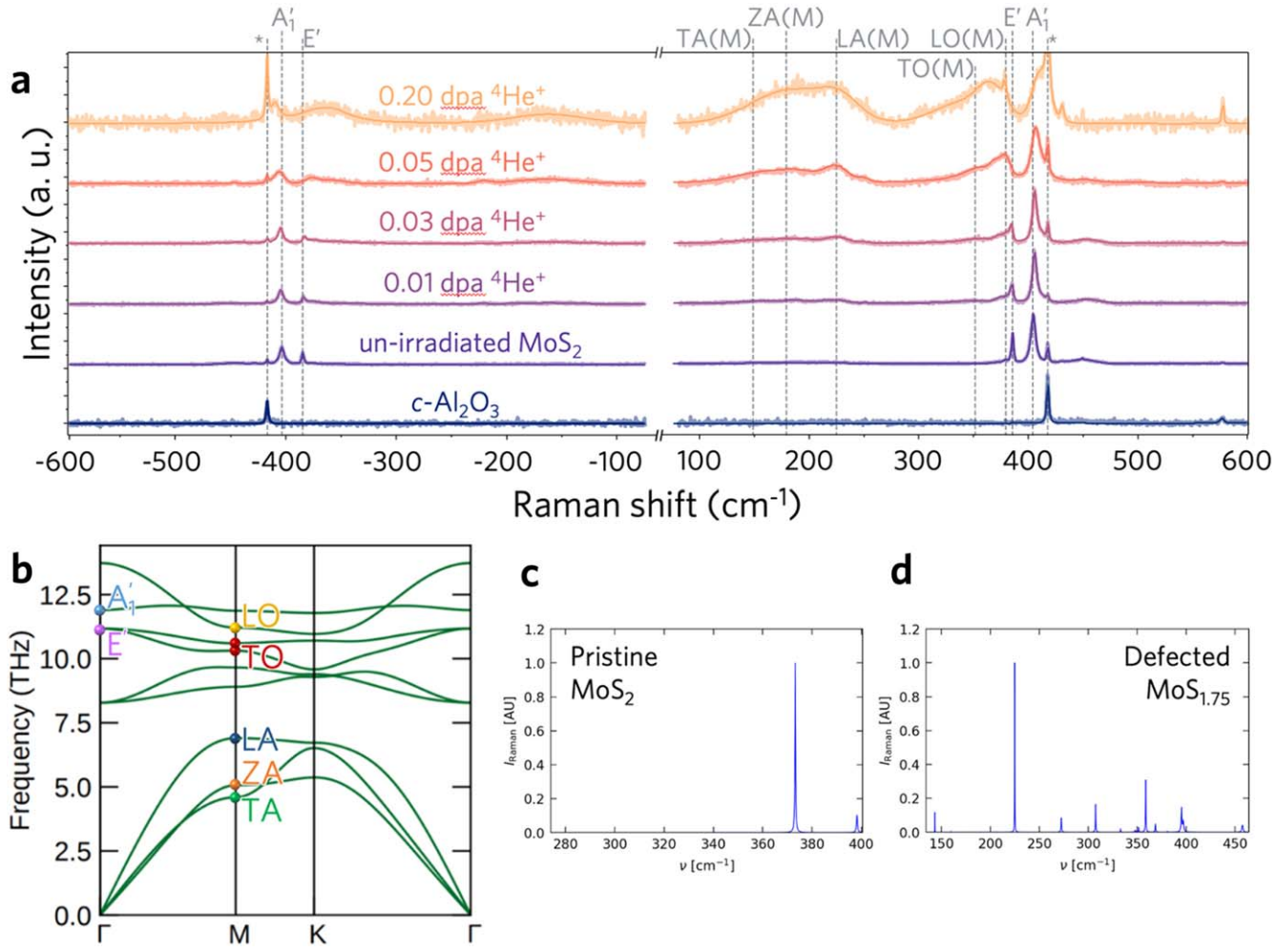

Figure 5. (a) Room temperature Stokes and anti-Stokes Raman spectroscopy of MoS_2 irradiated by $^4He^+$ ions with different fluences show the increase in intensities of defect peaks upon ion irradiation. The spectra are normalized to the A_1' for comparison with defect peaks, the *c*-Al_2O_3 peak is denoted by an asterisk. (b) Calculated phonon dispersion of pristine MoS_2. The optical and acoustic phonon modes that become Raman active upon introduction of defects are denoted. Calculated Raman spectra for (c) pristine strained MoS_2 and (d) MoS_2 with a S vacancy concentration of 2.7×10^{14} cm^{-2}., corresponding to $MoS_{1.75}$.

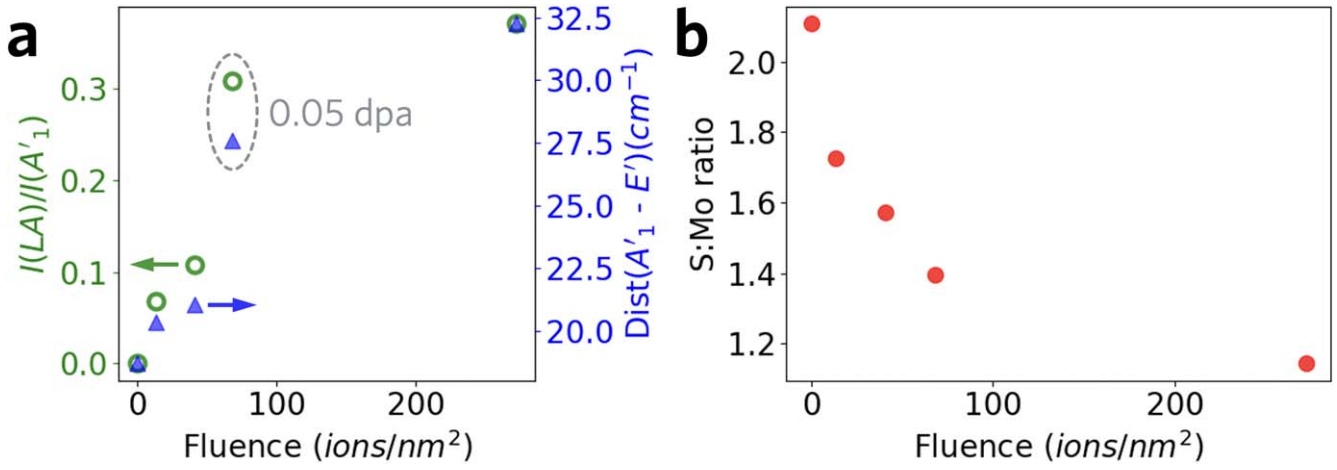

Figure 6. (a) Dependence of the ratio of Raman scattering intensities of the LA and A_1' modes (green circles) on the ion beam fluence. The fluence at 0.05 dpa $^4He^+$ shows in abnormally high intensity of both defect peaks and PL emission which could be result of unique ordering of defects. The evolution of the separation between the fitted A_1' and E′ peak positions (blue triangles) with increase in incident beam fluence. In unirradiated sample, the separation between the two peaks is 18.7 cm^{-1} (close to the values reported by other groups [62,63]) and the separation increases with an increase in incident ion fluence. (b) Dependence of S:Mo ratio on the fluence obtained by RBS. The ratio monotonically decreases with increase in ion fluence indicating that primarily, S vacancies would be generated by the incident beam.

corresponding to a beam fluence of 6.80×10^{15} ions cm^{-2}, showed exceedingly high PL intensity on the order of 200–600 times higher than the other irradiated samples (figure S3, supporting information). This broad PL peak (around 1.7 eV) may indicate an inhomogeneous distribution of a very high density of point defects which results in high amounts of radiative recombination centers for excitons. Large (several orders of magnitude) PL intensity increases have been seen for 2H-phase MoS_2 after chemical conversion to 1T-phase [54]. In our sensitive Raman characterization we are not able to distinguish the expected 1T-phase modes [55] from the defect-activated acoustic modes as could be the case for a trace 1T phases inside a defective 2H matrix. Additionally, previous studies on Carbon nanotubes also showed great increase in PL intensity due to formation of point defects. The point defects are believed to localize excitons and reduce non-radiative recombination [56,57]. Similarly, the creation of point defects could be reducing the probability of non-radiative recombination in the 0.05 dpa irradiated MoS_2 as well. Further combined theoretical and experimental studies on quantum states of defects with very gradual increase in the ion beam fluence are necessary to shed light on this topic.

Figure 4(b) gives the room-temperature TRPL analysis of both pristine and irradiated MoS_2 (0.05 dpa $^4He^+$) was carried out to investigate the carrier recombination dynamics. For the pristine sample, the initial fast decay component was within the 500 ps resolution limited by the instrument response function (479 $\pm$ 2 ps), which was consistent with previous reports claiming lifetime of intrinsic MoS_2 is below 100 ps [58,59]. Exciton-phonon scattering at room temperature leads to the observed slow decay component [60,61], which we obtain as 6.0 $\pm$ 0.2 ns for un-irradiated MoS_2. For the irradiated sample, a similar slow decay component with slightly increased lifetime of 7.7 $\pm$ 0.1 ns was observed. Surprisingly though, the initial fast decay time was significantly increased to 1.86 $\pm$ 0.02 ns, 1–2 orders slower than the PL decay of excitons in intrinsic MoS_2. The extended PL lifetime is attributed to exciton localization at the defect sites created by ion irradiation [60].

Figure 5(a) compares the Raman spectra of the pristine and irradiated MoS_2 samples taken at room temperature. A systematic increase in the intensity of acoustic (LA, TA, and ZA) and optical (TO and LO) peak intensities at the M-point of the Brillouin zone was seen with increasing ion fluence, as well as a blue shift of the A_1' peak and red shift of the E′ peak indicating the MoS_2 becomes increasingly tensile strained with increasing fluence. The changes in Raman spectra can be attributed to two factors: generation of defects and lattice straining. We have performed DFT calculations to differentiate the contribution of these two factors on the Raman spectra [figures 5(b)–(d)]. These calculations suggest that biaxial lattice straining would result in a shift of the A_1' and E_1 peaks but would not result in emergence of new peaks since straining does not lead to changes in vibrational symmetry. We did notice a slight blue-shift of the A_1' peak with fluence as can be seen in figure 4(a). On the other hand, introduction of lattice defects would result in drastic changes in the existing symmetry leading to more vibrational modes becoming Raman active. The optical and acoustic modes are inactive in defect free MoS_2 but are activated by generation of point defects due to ion irradiation. The ratio of LA to A_1' peak intensities is expected to increase linearly with defect density as [52]:

$$\frac{I(\mathrm{LA})}{I(\mathrm{A}_1')} = C_1/L_D^2 \tag{1}$$

$$L_D \propto 1/\sqrt{\sigma}, \tag{2}$$

Thus

$$\frac{I(\mathrm{LA})}{I(\mathrm{A}_1')} = C_2\sigma, \tag{3}$$

here, I(LA) and $I(A_1')$ are the scattering intensities of the LA and A_1' peaks respectively, C_1 and C_2 are proportionality constants, L_D is the average inter-defect distance, and σ is the ion irradiation fluence.

Upon plotting the ratio of intensities of defect-enabled LA peak and A_1' peak as a function of irradiation fluence, a strong linear dependence is observed [figure 6(a)]. As seen from the PL spectra, irradiation at 0.05 dpa $^4He^+$ gives rise to very high intensity of defect peak and is considered an outlier. The other intensity ratios of the other three fluences fall in a straight line with R^2 value of 0.99. Since ratio of peak intensity is directly correlated with defect density, this strong correlation between fluence and ratios of peak intensities is also indicative of the strong correlation between the fluence of irradiated ion beam and the resultant defect density. Thus, it can be inferred that precise defect engineering in wafers of 2D materials can be attained using this novel low power ion irradiation technique. The distance between the positions of A_1' and $_{E}'$ peaks is indicative of the strain in the lattice [64]. Separation of the two peaks, in wavenumber space, was found to increase as the ion fluence increased indicating that the strain in the sample increases proportionally to the ion fluence. RBS measurements of the stoichiometry of the irradiated samples [figure 6(b)] show that upon increasing the ion fluence, the S:Mo ratio steadily decreases. This indicates that irradiation primarily knocks out the S atoms, potentially creating S vacancy sites consistent with previous reports [38,65].

Conclusion

This study demonstrates that controllable defect generation in 2D materials can be achieved using a low power ion irradiation technique to control the optical emission properties while retaining underlying crystallinity without inducing phase changes. It is shown that small modification in the ion fluence can result in precise modulation of defect density in the sample; defect density being inversely correlated to square root of ion fluence. Optical spectra of defect free versus irradiated MoS_2 were explored to establish links between the changes in peak position and intensity with defect densities. Increasing fluence results in systematically increasing the intensity of defect peaks in the Raman spectra, the ratio of

defect peak to A_1' peak is established to be a good indicator of inter-defect distances. The photoluminescence spectra show emergence of bound exciton peaks upon ion irradiation. The exceedingly bright PL peak at beam fluence of 6.80×10^{15} ions cm^{-2} may be the result of unique synergistic effects between lattice defect, warranting further studies on the interplay between defects and exciton localization, and can shed light on interesting emergent phenomena owing defect engineering in the 2D lattice.

Acknowledgments

This work was supported by the Laboratory Directed Research and Development program of Los Alamos National Laboratory under project numbers 20210036DR (SP, MTP) and 20210782ER (MTP). Epitaxial synthesis of MoS_2 was carried out at The Pennsylvania State University 2D Crystal Consortium—Materials Innovation Platform (2DCC-MIP) facility was supported by NSF cooperative agreements DMR-1539916 and DMR-2039351 (MC, TC, JMR). This work was performed in part at the Center for Integrated Nanotechnologies, an Office of Science User Facility operated for the U.S. Department of Energy (DOE) Office of Science. Los Alamos National Laboratory, an affirmative action equal opportunity employer, is managed by Triad National Security, LLC for the U.S. Department of Energy's NNSA, under contract 89233218CNA000001. HH, HZ and YW acknowledge support from DOE BES award 'Deterministic Placement and Integration Quantum Defects'.

Data availability statement

The data that support the findings of this study are available upon reasonable request from the authors.

ORCID iDs

Joan Marie Redwing https://orcid.org/0000-0002-7906-452X
Michael Thompson Pettes https://orcid.org/0000-0001-6862-6841

References

[1] Chen K-S, Balla I, Luu N S and Hersam M C 2017 Emerging opportunities for two-dimensional materials in lithium-ion batteries *ACS Energy Lett.* **2** 2026
[2] Parida S, Mishra A, Chen J, Wang J, Dobley A, Carter C B and Dongare A M 2020 Vertically stacked 2H-1T dual-phase mos_2 microstructures during lithium intercalation: a first principles study *J. Am. Ceram. Soc.* **103** 6603
[3] Park H, Oh D S, Lee K J, Jung D Y, Lee S, Yoo S and Choi S-Y 2020 Flexible and transparent thin-film transistors based on two-dimensional materials for active-matrix display *ACS Appl. Mater. Interfaces* **12** 4749
[4] Kim S J, Choi K, Lee B, Kim Y and Hong B H 2015 Materials for flexible, stretchable electronics: graphene and 2D materials *Annu. Rev. Mater. Res.* **45** 63
[5] Liang M, Ali A, Belaidi A, Hossain M I, Ronan O, Downing C, Tabet N, Sanvito S, Ei-Mellouhi F and Nicolosi V 2020 Improving stability of organometallic-halide perovskite solar cells using exfoliation two-dimensional molybdenum chalcogenides *npj 2D Mater. Appl.* **4** 40
[6] Zhang H 2018 Introduction: 2D materials chemistry *Chem. Rev.* **118** 6089
[7] Qiu Q and Huang Z 2021 Photodetectors of 2D materials from ultraviolet to terahertz waves *Adv. Mater.* **33** 2008126
[8] Li X, Jones A C, Choi J, Zhao H, Chandrasekaran V, Pettes M T, Piryatinski A, Sinitsyn N, Crooker S A and Htoon H 2022 Proximity induced chiral quantum light generation in strain-engineered $WSe_2/NiPS_3$ heterostructures *arXiv* [cond-mat. mes-hall] (https://doi.org/10.48550/arXiv.2203.00797)
[9] Zhao H, Pettes M T, Zheng Y and Htoon H 2021 Site-controlled telecom-wavelength single-photon emitters in atomically-thin $MoTe_2$ *Nat. Commun.* **12** 6753
[10] Wu W, Morales-Acosta M D, Wang Y and Pettes M T 2019 Isotope effect in bilayer WSe_2 *Nano Lett.* **19** 1527
[11] Wu W, Dass C K, Hendrickson J R, Montaño R D, Fischer R E, Zhang X, Choudhury T H, Redwing J M, Wang Y and Pettes M T 2019 Locally defined quantum emission from epitaxial few-layer tungsten diselenide *Appl. Phys. Lett.* **114** 213102
[12] Yu L, Deng M, Zhang J L, Borghardt S, Kardynal B, Vučković J and Heinz T F 2021 Site-controlled quantum emitters in monolayer $MoSe_2$ *Nano Lett.* **21** 2376
[13] Rosenberger M R, Dass C K, Chuang H-J, Sivaram S V, McCreary K M, Hendrickson J R and Jonker B T 2019 Quantum calligraphy: Writing single-photon emitters in a two-dimensional materials platform *ACS Nano* **13** 904
[14] Palacios-Berraquero C, Kara D M, Montblanch A R P, Barbone M, Latawiec P, Yoon D, Ott A K, Loncar M, Ferrari A C and Atatüre M 2017 Large-scale quantum-emitter arrays in atomically thin semiconductors *Nat. Commun.* **8** 15093
[15] Branny A, Kumar S, Proux R and Gerardot B D 2017 Deterministic strain-induced arrays of quantum emitters in a two-dimensional semiconductor *Nat. Commun.* **8** 15053
[16] He Y-M *et al* 2015 Single quantum emitters in monolayer semiconductors *Nat. Nanotechnol.* **10** 497
[17] Jiang H, Zheng L, Liu Z and Wang X 2020 Two-dimensional materials: From mechanical properties to flexible mechanical sensors *Info. Mat.* **2** 1077
[18] Wu W, Wang J, Ercius P, Wright N C, Leppert-Simenauer D M, Burke R A, Dubey M, Dongare A M and Pettes M T 2018 Giant mechano-optoelectronic effect in an atomically thin semiconductor *Nano Lett.* **18** 2351
[19] Xia F, Wang H, Xiao D, Dubey M and Ramasubramaniam A 2014 Two-dimensional material nanophotonics *Nat. Photon.* **8** 899
[20] Akinwande D, Petrone N and Hone J 2014 Two-dimensional flexible nanoelectronics *Nat. Commun.* **5** 5678
[21] Liu X and Hersam M C 2019 2D materials for quantum information science *Nat. Rev. Mater.* **4** 699
[22] Radisavljevic B, Radenovic A, Brivio J, Giacometti V and Kis A 2011 Single-layer MoS_2 transistors *Nat. Nanotechnol.* **6** 147
[23] 2022 *Materials Commodity Summaries* (Reston, Virginia: United States Geological Survey) http://minerals.usgs.gov/minerals/pubs/mcs/2014/mcs2014.pdf (https://doi.org/10.3133/mcs2022)
[24] Ganatra R and Zhang Q 2014 Few-layer MoS_2: a promising layered semiconductor *ACS Nano* **8** 4074

[25] Mak K F, Lee C, Hone J, Shan J and Heinz T F 2010 Atomically thin MoS_2: a new direct-gap semiconductor *Phys. Rev. Lett.* **105** 136805

[26] Tongay S *et al* 2013 Defects activated photoluminescence in two-dimensional semiconductors: Interplay between bound, charged and free excitons *Sci. Rep.* **3** 2657

[27] Nan H *et al* 2014 Strong photoluminescence enhancement of MoS_2 through defect engineering and oxygen bonding *ACS Nano* **8** 5738

[28] Ghorbani-Asl M, Kretschmer S, Spearot D E and Krasheninnikov A V 2017 Two-dimensional MoS_2 under ion irradiation: From controlled defect production to electronic structure engineering *2D Mater.* **4** 025078

[29] Xie J, Zhang H, Li S, Wang R, Sun X, Zhou M, Zhou J, Lou X W and Xie Y 2013 Defect-rich MoS_2 ultrathin nanosheets with additional active edge sites for enhanced electrocatalytic hydrogen evolution *Adv. Mater.* **25** 5807

[30] Li D, Zhao L, Xia Q, Wang J, Liu X, Xu H and Chou S 2022 Activating MoS_2 nanoflakes via sulfur defect engineering wrapped on CNTs for stable and efficient Li-O_2 batteries *Adv. Funct. Mater.* **32** 2108153

[31] Xie Y, Liang F, Chi S, Wang D, Zhong K, Yu H, Zhang H, Chen Y and Wang J 2020 Defect engineering of MoS_2 for room-temperature terahertz photodetection *ACS Appl. Mater. Interfaces* **12** 7351

[32] Wu K, Li Z, Tang J, Lv X, Wang H, Luo R, Liu P, Qian L, Zhang S and Yuan S 2018 Controllable defects implantation in MoS_2 grown by chemical vapor deposition for photoluminescence enhancement *Nano Res.* **11** 4123

[33] Ye G, Gong Y, Lin J, Li B, He Y, Pantelides S T, Zhou W, Vajtai R and Ajayan P M 2016 Defects engineered monolayer MoS_2 for improved hydrogen evolution reaction *Nano Lett.* **16** 1097

[34] Fox D S *et al* 2015 Nanopatterning and electrical tuning of MoS_2 layers with a subnanometer helium ion beam *Nano Lett.* **15** 5307

[35] Ma Q *et al* 2014 Postgrowth tuning of the bandgap of single-layer molybdenum disulfide films by sulfur/selenium exchange *ACS Nano* **8** 4672

[36] Kwon S, Choi S H, Kim Y J, Yoon I T and Yang W 2018 Proton beam flux dependent work function of mono-layer MoS_2 *Thin Solid Films* **660** 766

[37] Wang B, Yang S, Chen J, Mann C, Bushmaker A and Cronin S B 2017 Radiation-induced direct bandgap transition in few-layer MoS_2 *Appl. Phys. Lett.* **111** 131101

[38] He Z *et al* 2018 Defect engineering in single-layer MoS_2 using heavy ion irradiation *ACS Appl. Mater. Interfaces* **10** 42524

[39] Mathew S *et al* 2012 Magnetism in MoS_2 induced by proton irradiation *Appl. Phys. Lett.* **101** 102103

[40] Valerius P *et al* 2020 Reversible crystalline-to-amorphous phase transformation in monolayer MoS_2 under grazing ion irradiation *2D Mater.* **7** 025005

[41] Wu X and Zhu X 2021 Molecular dynamics simulations of ion beam irradiation on graphene/MoS_2 heterostructure *Sci. Rep.* **11** 21113

[42] Wu X, Zhu X and Lei B 2021 Impact of ion beam irradiation on two-dimensional MoS_2: a molecular dynamics simulation study *J. Phys. Condens. Matter* **34** 055402

[43] Han S W, Yun W S, Kang M, Lee S and Park J 2022 Phase transition of a MoS_2 monolayer through top layer desulfurization by He^+ ion irradiation *J. Appl. Phys.* **131** 224301

[44] Rose P H and Ryding G 2006 Concepts and designs of ion implantation equipment for semiconductor processing *Rev. Sci. Instrum.* **77** 111101

[45] Li H, Liu C, Zhang Y, Wang T, Zhang H, Li P, Qi C, Huo M and Dong S 2022 Effects of N-ion implantation on the electrical and photoelectronic properties of MoS_2 field effect transistors *Phys. Status Solidi* A **219** 2100551

[46] Solin S A and Ramdas A K 1970 Raman spectrum of diamond *Phys. Rev.* B **1** 1687

[47] Kresse G and Hafner J 1993 *Ab initio* molecular dynamics for liquid metals *Phys. Rev.* B **47** 558

[48] Perdew J P, Burke K and Ernzerhof M 1996 Generalized gradient approximation made simple *Phys. Rev. Lett.* **77** 3865

[49] Blöchl P E 1994 Projector augmented-wave method *Phys. Rev.* B **50** 17953

[50] Togo A and Tanaka I 2015 First principles phonon calculations in materials science *Scr. Mater.* **108** 1

[51] Londoño-Calderon A, Dhall R, Ophus C, Schneider M M, Wang Y, Dervishi-Whetham E, Kang H S, Lee C-H, Yoo J and Pettes M T 2022 Visualizing grain statistics in MOCVD WSe_2 through four-dimensional scanning transmission electron microscopy *Nano Lett.* **22** 2578

[52] Mignuzzi S, Pollard A J, Bonini N, Brennan B, Gilmore I S, Pimenta M A, Richards D and Roy D 2015 Effect of disorder on Raman scattering of single-layer MoS_2 *Phys. Rev.* B **91** 195411

[53] McCreary K M, Hanbicki A T, Sivaram S V and Jonker B T 2018 A- and B-exciton photoluminescence intensity ratio as a measure of sample quality for transition metal dichalcogenide monolayers *APL Mater.* **6** 111106

[54] Xia Z, Tao Y, Pan Z and Shen X 2019 Enhanced photocatalytic performance and stability of 1T MoS_2 transformed from 2H MoS2 via Li intercalation *Results Phys.* **12** 2218

[55] Attanayake N H, Thenuwara A C, Patra A, Aulin Y V, Tran T M, Chakraborty H, Borguet E, Klein M L, Perdew J P and Strongin D R 2018 Effect of intercalated metals on the electrocatalytic activity of 1T-MoS_2 for the hydrogen evolution reaction *ACS Energy Lett.* **3** 7

[56] Wang B, Shen L, Yang S, Chen J, Echternach J, Dhall R, Kang D and Cronin S 2018 Defect-induced photoluminescence enhancement and corresponding transport degradation in individual suspended carbon nanotubes *Phys. Rev. Appl.* **9** 054022

[57] Piao Y, Meany B, Powell L R, Valley N, Kwon H, Schatz G C and Wang Y 2013 Brightening of carbon nanotube photoluminescence through the incorporation of sp^3 defects *Nat. Chem.* **5** 840

[58] Korn T, Heydrich S, Hirmer M, Schmutzler J and Schüller C 2011 Low-temperature photocarrier dynamics in monolayer MoS_2 *Appl. Phys. Lett.* **99** 102109

[59] Amani M *et al* 2015 Near-unity photoluminescence quantum yield in MoS_2 *Science* **350** 1065

[60] Moody G, Tran K, Lu X, Autry T, Fraser J M, Mirin R P, Yang L, Li X and Silverman K L 2018 Microsecond valley lifetime of defect-bound excitons in monolayer WSe_2 *Phys. Rev. Lett.* **121** 057403

[61] Li H and Zhang X H 2020 Temperature-dependent photoluminescence and time-resolved photoluminescence study of monolayer molybdenum disulfide *Opt. Mater.* **107** 110150

[62] Li H, Zhang Q, Yap C C R, Tay B K, Edwin T H T, Olivier A and Baillargeat D 2012 From bulk to monolayer MoS_2: Evolution of Raman scattering *Adv. Funct. Mater.* **22** 1385

[63] Taube A, Judek J, Jastrzębski C, Duzynska A, Świtkowski K and Zdrojek M 2014 Temperature-dependent nonlinear phonon shifts in a supported MoS_2 monolayer *ACS Appl. Mater. Interfaces* **6** 8959

[64] Conley H J, Wang B, Ziegler J I, Haglund R F, Pantelides S T and Bolotin K I 2013 Bandgap engineering of strained monolayer and bilayer MoS_2 *Nano Lett.* **13** 3626

[65] Kim H-J, Yun Y J, Yi S N, Chang S K and Ha D H 2020 Changes in the photoluminescence of monolayer and bilayer molybdenum disulfide during laser irradiation *ACS Omega* **5** 7903